Atmos. Chem. Phys., 18, 4639–4656, 2018
https://doi.org/10.5194/acp-18-4639-2018

Atmospheric Chemistry and Physics Open Access EGU

Sources and physicochemical characteristics of black carbon aerosol from the southeastern Tibetan Plateau: internal mixing enhances light absorption

Qiyuan Wang[1], Junji Cao[1,2], Yongming Han[1,3], Jie Tian[4], Chongshu Zhu[1], Yonggang Zhang[1], Ningning Zhang[1], Zhenxing Shen[4], Haiyan Ni[1], Shuyu Zhao[1], and Jiarui Wu[1]

[1]Key Laboratory of Aerosol Chemistry and Physics, State Key Laboratory of Loess and Quaternary Geology, Institute of Earth Environment, Chinese Academy of Sciences, Xi'an, 710061, China
[2]Institute of Global Environmental Change, Xi'an Jiaotong University, Xi'an, 710049, China
[3]School of Human Settlements and Civil Engineering, Xi'an Jiaotong University, Xi'an, 710049, China
[4]Department of Environmental Science and Engineering, School of Energy and Power Engineering, Xi'an Jiaotong University, Xi'an, 710049, China

Correspondence: Qiyuan Wang (wangqy@ieecas.cn) and Junji Cao (cao@loess.llqg.ac.cn)

Received: 28 August 2017 – Discussion started: 21 November 2017
Revised: 15 February 2018 – Accepted: 6 March 2018 – Published: 5 April 2018

Abstract. Black carbon (BC) aerosol has important effects on the climate and hydrology of the Tibetan Plateau (TP). An intensive measurement campaign was conducted at Lulang (∼ 3300 m a.s.l. – above sea level), southeastern TP, from September to October 2015, to investigate the sources and physicochemical characteristics of refractory BC (rBC) aerosol. The average rBC mass concentration was $0.31 \pm 0.55\,\mu g\,m^{-3}$, which is higher than most prior results for BC on the TP. A clear diurnal cycle in rBC showed high values in the morning and low values in the afternoon. A bivariate polar plot showed that rBC loadings varied with wind speed and direction, which also reflected the dominant transport direction. The estimated net surface rBC transport intensity was $+0.05 \pm 0.29\,\mu g\,s^{-1}\,m^{-2}$, indicating stronger transport from outside the TP compared with its interior. Cluster analysis and a concentration-weighted trajectory model connected emissions from north India to the high rBC loadings, but the effects of internal TP sources should not be overlooked. The average mass median diameter (MMD) of rBC was 160 ± 23 nm, with smaller MMDs on rainy days (145 nm) compared with non-rainy days (164 nm). The average number fraction of thickly coated rBC (F_{rBC}) was 39 ± 8 %, and it increased with the O_3 mixing ratios from 10:00 to 14:00 LT, indicating that photochemical oxidation played a role in forming rBC coatings. The average rBC absorption enhancement (E_{abs}) was estimated to be 1.9, suggesting that light absorption by coated rBC particles was greater than for uncoated ones. The E_{abs} was strongly positively correlated with the F_{rBC}, indicating an amplification of light absorption for internally mixed rBC. For rBC cores < 170 nm, E_{abs} was negatively correlated with MMD, but it was nearly constant for rBC cores > 170 nm. Our study provides insight into the sources and evolution of rBC aerosol on the TP, and the results should be useful for improving models of the radiative effects of carbonaceous aerosols in this area.

1 Introduction

The Tibetan Plateau (TP) is the world's largest high-elevation region. It holds the largest ice mass on the planet outside the polar regions and is sometimes called the Earth's "Third Pole" (Yao et al., 2008). The snow and associated glacial meltwater on the TP provides fresh water for drinking and irrigation for more than 1 billion people downstream (Immerzeel et al., 2010). The TP exerts significant thermal and dynamic impacts on hydrological processes in South and East Asia. For example, changes in the area covered by glaciers and snowpack on the TP affect the heat fluxes and water exchange between the atmosphere and the earth's surface, and that, in turn, affects the atmospheric circulation

associated with the Asian Monsoon System (Lau and Kim, 2006). Glaciers can be sensitive to climate change (Dyurgerov and Meier, 2000), and recent observations have shown a continuing retreat in Tibetan glaciers (e.g., Xu et al., 2009; Yao et al., 2012; Zhang et al., 2012; Loibl et al., 2014; Kang et al., 2015; Huintjes et al., 2016; Ke et al., 2017). For instance, Yao et al. (2012) reviewed the status of glaciers on the TP and surrounding areas over the past 30 years. These authors reported systematic differences from region to region, and their study showed that the greatest reduction in glacial length and area and the most negative mass balance occurred in the Himalayas (excluding the Karakorum).

The past few decades have witnessed rapid growth in the human population and industrialization in South and East Asia, and this growth has led to widespread air pollution (Vadrevu et al., 2014; Cao, 2017). An important component of this pollution is the black carbon (BC) aerosol, the light-absorbing, refractory material produced mainly through the incomplete combustion of fossil fuels and biomass (Bond et al., 2013). In addition to its effects on air quality, BC plays a unique and important role in the Earth's climate system due to its impacts on solar radiation, clouds, and snow albedo (Bond et al., 2013). Indeed, it has been suggested that BC is the second largest contributor to anthropogenic radiative forcing after carbon dioxide due to its strong absorption of solar radiation (Jacobson, 2001; Ramanathan and Carmichael, 2008; Bond et al., 2013). Furthermore, BC aerosol can alter atmospheric circulation patterns, accelerate snowmelt, and cause glaciers to retreat (Xu et al., 2009).

Geographically, the TP is surrounded by South and East Asia where BC sources are strong (Zhang et al., 2009), and the TP has become impacted by these high-BC source areas due to the general circulation patterns (Cao et al., 2010; Lu et al., 2012; S. Zhao et al., 2017). For example, Lu et al. (2012) found that BC loadings in the Himalayas and TP increased by 41 % from 1996 to 2010 due to the influences of surrounding areas. Annually, on average, South and East Asia account for 67 and 17 % of BC transported to the plateau, respectively. However, several recent studies showed that the impact of internal Tibetan sources (e.g., yak dung combustion by local residents) on the atmosphere of the TP should not be overlooked (Chen et al., 2015; Li et al., 2016a; X. Zhang et al., 2017). In the past few decades, a number of field campaigns conducted on the TP have investigated the concentrations, sources, and spatial and temporal variations of BC aerosol (e.g., Engling et al., 2011; Cong et al., 2015; M. Wang et al., 2016; Zhu et al., 2016; Wang et al., 2017; Z. Zhao et al., 2017). Recently, research has begun to focus on the light absorption characteristics of BC particles in the atmosphere and snow (Li et al., 2016b, c; Y. Zhang et al., 2017). These studies have been helpful for improving estimates of the radiative forcing of BC in the atmosphere of the TP.

Although some aerosol-related field studies have been conducted on the TP, the BC measurements were mainly made using online or offline filter-based techniques (e.g., aethalometer, thermal/optical reflectance method, and multi-angle absorption photometer) (e.g., Engling et al., 2011; Marinoni et al., 2010; Wan et al., 2015; Zhu et al., 2016; Li et al., 2017). These techniques are based on the bulk particle deposition onto the filters, and they cannot provide high time resolution information on of BC size and mixing state. This is a significant limitation of the filter-based methods because the optical properties of the BC aerosol are related to the particles' chemical and microphysical characteristics, including their size and mixing state. For instance, Liu et al. (2015) reported direct evidence of substantial field-measured BC absorption enhancement (E_{abs}) in an urban area, and this was strongly dependent on the internal mixing of BC. Peng et al. (2016) used a novel environmental chamber to quantify the aging and variations in the morphology and optical properties of BC particles from Beijing, China, and Houston, United States. That study showed that BC particles initially changed from a fractal to spherical morphology with little change in absorption followed by growth into compact particles with large E_{abs}.

Accurate information on the physicochemical characteristics of BC can improve our understanding of anthropogenic climate impacts on the TP, but there is still a lack of high time resolution measurements on the size and mixing state of BC in this region. This deficiency has led to considerable uncertainty in the calculations of BC direct radiative forcing over TP (He et al., 2014). In this study, we used a single-particle soot photometer (SP2) and a photoacoustic extinctiometer (PAX) to determine the mass concentrations, size distributions, mixing states, and light absorption properties of refractory BC (rBC) from the southeastern part of the TP. Various terms have been used in the literature for the most refractory and light-absorbing components of carbonaceous aerosols, and these have been based on the experimental measurement techniques (Bond et al., 2013). Here the term rBC is used exclusively in reference to SP2 measurements, while eBC (equivalent BC) and EC (elemental carbon) refer to the data from the optical absorption method and the thermal heating and optical absorption techniques, respectively, used in other studies (Petzold et al., 2013). The primary objectives of this study were (1) to investigate the effects of meteorology on rBC and identify probable source regions responsible for the high rBC loadings; (2) to characterize the rBC size distributions and the evolution of rBC mixing state; and (3) to derive the rBC E_{abs} and evaluate the factors that affect it.

2 Methodology

2.1 Sampling site

Physicochemical and optical properties of rBC aerosol were measured in samples collected from a remote area of Lulang, which is located on the southeastern part of the TP (Fig. 1). An intensive measurement campaign was conducted from

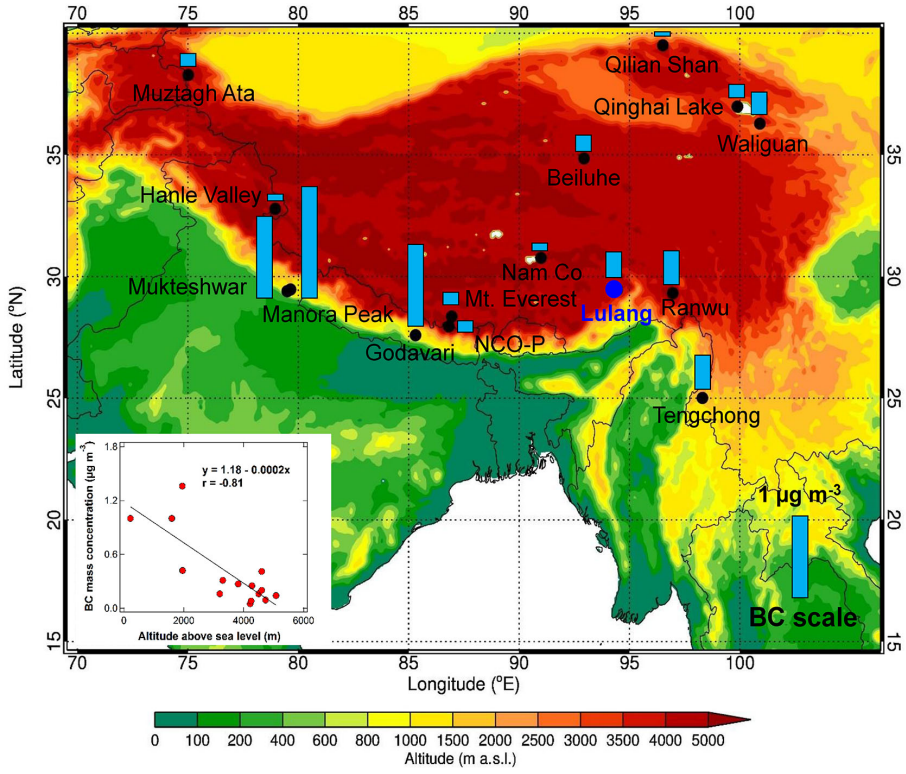

Figure 1. Black carbon concentrations ($\mu g\,m^{-3}$) measured at 15 sampling sites in the Himalayas and on the Tibetan Plateau based on the measurements from this study (blue solid circles) and other studies (black solid circles) from Ma et al. (2003), Pant et al. (2006), Marinoni et al. (2010), Stone et al. (2010), Babu et al. (2011), Engling et al. (2011), Zhao et al. (2012), Li et al. (2017), Wan et al. (2015), Wang et al. (2015a), M. Wang et al. (2016), Zhu et al. (2016), and Raatikainen et al. (2017). More detailed information concerning these studies is summarized in Table S1. The inset is a scatter plot of the mass concentrations of BC versus the altitude of each sampling site. The map in the figure was drawn using the Weather Research and Forecasting (WRF) model.

17 September to 31 October 2015 on the dormitory rooftop of the Southeast Tibet Integrated Observation and Research Station for the Alpine Environment, Chinese Academy of Sciences (94.44° E, 29.46° N; ∼ 3300 m a.s.l. – above sea level). There were no major anthropogenic sources near the sampling site.

2.2 Data collection

2.2.1 Quantification of rBC mass, size, and mixing state

A single-particle soot photometer manufactured by Droplet Measurement Technologies (Boulder, CO, USA) was used to determine the mass, size, and mixing state of rBC particles. The operation and principles of the SP2 have been described in detail elsewhere (Schwarz et al., 2006). Briefly, a high-intensity intra-cavity Nd:YAG laser operating at wavelength of 1064 nm heated an individual rBC-containing particle to its incandescence temperature (∼ 4000 K), which then emitted thermal radiation that was detected optically. Simultaneously, the laser light scattered by the rBC-containing particle was detected elastically. The intensity of the incandescence signal is proportional to the mass of rBC contained in the particle, but it is not affected by the particle morphology or the presence of non-refractory matter (Slowik et al., 2007). In this study, the SP2 was calibrated with a standard fullerene soot sample (Lot F12S011, Alfa Aesar, Inc., Ward Hill, MA, USA). A linear relationship was established between the peak intensity of the incandescence signal and the rBC mass. For this procedure, fullerene soot particles generated by an atomizer (Model 9302, TSI Inc., Shoreview, MN, USA) were passed through a diffusion silica-gel dryer, and then they were separated by size with a differential mobility analyzer (Model 3080, TSI Inc.) before entering the SP2 instrument. The corresponding fullerene soot masses were estimated using the effective density data provided by Gysel et al. (2011). More information concerning the SP2 calibration procedure may be found in Wang et al. (2014).

The measured rBC mass was converted to the volume equivalent diameter (VED) by assuming rBC particles were solid spheres with a density of $1.8\,g\,cm^{-3}$ (Bond and Bergstrom, 2006). The detection efficiency of the SP2 drops off for rBC core sizes $< \sim 70$ nm, and the signal becomes saturated for sizes $> \sim 600$ nm. Based on a mono-modal log-normal fit for the mass size distributions as described in

Sect. 3.3.1 below (Fig. S1 in the Supplement), the reported rBC mass concentrations in this study were scaled up by a factor of ∼ 1.1 to compensate for the losses outside of the SP2 detection range. The uncertainty of the SP2 mass measurements was ∼ 20 %, which was estimated by propagating the uncertainties caused by the SP2 response to ambient rBC mass (∼ 15 %; Laborde et al., 2012), sample flow (∼ 10 %), and estimates of the rBC mass beyond the SP2 detection range (∼ 10 %).

A major advantage of the SP2 is that it has the capability of determining the rBC mixing state (Schwarz et al., 2006). Freshly emitted rBC can be internally mixed with non-rBC materials through the process of gas–particle conversion. When the laser beam in the SP2 heats an internally mixed rBC particle, the coatings are preferentially evaporated, and that causes a decrease in the intensity of the scattering signal. After that, the rBC core starts to vaporize and that produces a peak in the incandescence signal. Therefore, there is a lag time between the peaks of the scattering and incandescence signals. These lag times can be used to characterize the internal mixing of rBC (McMeeking et al., 2011; Huang et al., 2012; Wu et al., 2016). Figure S2 shows that the lag times exhibited a bimodal distribution, with ∼ 2 µs separating two distinct populations. The rBC-containing particles with a lag time > 2 µs were considered to have substantial coatings, and those particles were denoted as thickly coated. In contrast, the rBC-containing particles with lag times < 2 µs were classified as uncoated or thinly coated. Here the number fraction of thickly coated rBC (F_{rBC}) was used to represent the degree of internal mixing of the rBC particles, and it was calculated by dividing the number of thickly coated rBC particles by the total number of rBC particles. As there were no incandescence signals detected for small particles and the scattering signal became saturated for large coated rBC particles, the rBC core sizes used to evaluate internal mixing were limited to ∼ 70 to 300 nm VED. An examination of the number size distribution of rBC shows that this was not a critical limitation in the following analysis because that size range contained the vast majority of the detected rBC particles (see Fig. S1).

2.2.2 Particle light absorption measurements

A photoacoustic extinctiometer operating at a wavelength of 870 nm (PAX_{870}, Droplet Measurement Technologies) was used to measure the particles' light absorption coefficients (b_{abs}) based on intra-cavity photoacoustic technology. The light-absorbing particles were heated by the laser beam in the acoustic chamber. This heating produced a pressure wave that was detected with a sensitive microphone. The PAX_{870} can also measure the particles' light scattering coefficient (b_{scat}) simultaneously with a wide-angle integrating reciprocal nephelometer in the scattering chamber. Before and during sampling, the light scattering and absorption of the PAX_{870} were calibrated with ammonium sulfate and freshly generated propane soot, respectively. The light extinction coefficient ($b_{ext} = b_{scat} + b_{abs}$) can be calculated from the laser power of the PAX_{870}. Thus a correction factor can be established from the relationship between the calculated b_{abs} ($= b_{ext} - b_{scat}$) and the measured b_{abs}. The b_{ext} is calculated using the following formula:

$$b_{ext} = -\frac{1}{0.354} \times \ln \frac{I}{I_0} \times 10^6 \left[\mathrm{Mm}^{-1}\right], \quad (1)$$

where 0.354 is the path length of the laser beam through the cavity in m; 10^6 is a conversion factor used to express b_{ext} in Mm^{-1}; I is the laser power during calibration (mW), and I_0 is the average laser power before and after calibration. A linear relationship was established between the extinction-minus-scattering coefficients and the measured b_{abs}. The slope of the regression line, that is, the correction factor, was then used as the new calibration factor for absorption. In this study, the same steps for the absorption calibration were repeated until the correction factor was stable within ∼ 10 %. Different concentration gradients of freshly generated propane soot were used to give an absorption reading of ∼ 10 to 16 700 Mm^{-1} for absorption calibration (Fig. S3). The uncertainty of the PAX for absorption measurements was estimated to be ∼ 15 % based on the variations of b_{abs} caused by the noise during the sampling period. It is worth noting that the b_{scat} produced by freshly generated propane soot particles has a substantial contribution to b_{ext}, while ammonium sulfate is the only material that generates b_{scat}. Thus, the scattering was calibrated before the b_{abs} calibration using the same procedures as for the absorption calibration (Fig. S3). In this study, sampled particles passed through a Nafion® dryer (MD-110-48S; Perma Pure, Inc., Lakewood, NJ, USA) before entering the PAX_{870}. As shown in Fig. S4, the light-absorbing particle loss for this type of Nafion tube may be ∼ 10 %. Thus, the b_{abs} values were scaled up by a factor of ∼ 1.1 to compensate for the losses. Moreover, about 15 % of the total number of b_{abs} measurements were excluded because the values were lower than the minimum detection limit of PAX_{870} (1.0 Mm^{-1}).

2.2.3 Complementary data

A portable DustTrak™ aerosol monitor (Model 8530, TSI Inc., Shoreview, MN, USA) was used to measure the mass concentrations of total suspended particulate matter (TSP). Hourly ozone (O_3) was measured using a UV-based dual beam O_3 monitor (2B Technology model 205, CO, USA). Wind speed and wind direction were measured hourly with the use of an automatic weather station installed at the Southeast Tibet Integrated Observation and Research Station for the Alpine Environment, Chinese Academy of Sciences. The planetary boundary layer (PBL) heights were obtained from the European Centre for Medium-range Weather Forecasts (ECMWF). These can be downloaded from ERA-Interim (January 1979–present) reanalysis datasets at http:

//apps.ecmwf.int/datasets. The spatial distribution of the BC column mass density was retrieved from the Modern-Era Retrospective analysis for Research and Applications version 2 (MERRA-2) using the Goddard Earth Observing System Model, Version 5 (GEOS-5) with its Atmospheric Data Assimilation System, version 5.12.4 (https://giovanni.gsfc.nasa.gov/giovanni). True color images obtained from the Moderate Resolution Imaging Spectroradiometer (MODIS) on the Terra satellite were used to assess the pollution distributions visually on several selected days, and those images were downloaded from the website https://lance.modaps.eosdis.nasa.gov.

2.3 Data analysis

2.3.1 Assessment of surface transport

Hourly rBC concentrations and the corresponding wind data were used to estimate the surface transport of rBC at the Lulang site using the following formula (White et al., 1976):

$$f = \frac{1}{n}\sum_{j=1}^{n} C_j \times \mathrm{WS}_j \times \cos\theta_j, \tag{2}$$

where f is the surface transport intensity of rBC in units of $\mu g\,s^{-1}\,m^{-2}$ (that is, mass transported per unit time and area); C_j and WS_j are the mean rBC concentrations ($\mu g\,m^{-3}$) and wind speeds ($m\,s^{-1}$) during the jth observation hour, respectively; θ_j is the angle between wind direction and the north–south direction during the jth observation hour; and n is the total number of observation hours. Generally, strong winds favor the dispersion of air pollutants for local emission sources, whereas weak winds lead to accumulation. In contrast, for regional sources, strong winds can transport pollutants from upwind areas and cause high concentrations of pollutants downwind. Therefore, in this study, we viewed the surface flux intensity as a measure of the influence of regional transport in South Asia, and more specifically on the Lulang site using ground-based observations. Positive values for f were considered indicative of transport from outside the TP (e.g., the Indo-Gangetic Plain, IGP, and Bangladesh), whereas negative values indicated transport from the interior of the TP.

2.3.2 Cluster analysis of air-mass trajectories

Three-day air mass trajectories calculated backwards in time were used to characterize the atmospheric transport of rBC to Lulang. Each trajectory was calculated for an arrival height of 150 m above ground. The trajectories were calculated hourly using the Hybrid Single-Particle Lagrangian Integrated Trajectory (HYSPLIT) model (Draxler and Rolph, 2003) developed by the Air Resource Lab (ARL) of the National Oceanic and Atmospheric Administration (NOAA). Because a large number of trajectories (887) retrieved for the entire campaign showed diverse pathways, a clustering procedure was used to establish representative pathways for the trajectories based on an angle-based distance statistics method. This was defined using the law of cosines from the following equations (Sirois and Bottenheim, 1995):

$$d_{12} = \frac{1}{n}\sum_{i=1}^{n} \cos^{-1}\left(0.5 \times \frac{A_i + B_i - C_i}{\sqrt{A_i B_i}}\right) \tag{3}$$

$$A_i = (X_1(i) - X_0)^2 + (Y_1(i) - Y_0)^2 \tag{4}$$

$$B_i = (X_2(i) - X_0)^2 + (Y_2(i) - Y_0)^2 \tag{5}$$

$$C_i = (X_2(i) - X_1(i))^2 + (Y_2(i) - Y_1(i))^2, \tag{6}$$

where d_{12} is the mean angle between the two backward trajectories, which varies between 0 and π; X_0 and Y_0 represent the position of the receptor site (Lulang in the present case); and X_1 (Y_1) and X_2 (Y_2) refer to backward trajectories 1 and 2, respectively. A two-step algorithm was used to produce the clusters. First, a Hartigan's K mean algorithm was used to construct several clusters of backward trajectories. Those clusters were then examined visually, and selected backward trajectories were moved from one cluster to another in order to define clusters that were easier to interpret with respect to geographical and/or anthropogenic source regions. In this study, three clusters were chosen as representative of the backward trajectory clusters. The simulation was conducted using the GIS-based TrajStat software (Wang et al., 2009).

2.3.3 Concentration-weighted trajectory (CWT) model

A CWT model was used to construct the spatial distribution of the rBC sources that potentially influenced the air sampled at Lulang. For the CWT calculations, the entire geographic region covered by the 3-day backward trajectories was separated into ~8100 grid cells of 0.5° latitude × 0.5° longitude. Each grid cell was assigned a residence-time-weighted concentration obtained by the hourly averaged rBC concentration associated with the trajectories that crossed that grid cell (Hsu et al., 2003):

$$C_{ij} = \frac{\sum_{l=1}^{M} C_l \tau_{ijl}}{\sum_{l=1}^{M} \tau_{ijl}}, \tag{7}$$

where C_{ij} is the average weighted concentration in the ijth grid cell; C_l is the measured rBC concentration on the arrival of trajectory l; τ_{ijl} is the number of trajectory endpoints in the ijth grid cell by trajectory l; and M is the total number of trajectories. A high C_{ij} value indicates that air parcels that traveled over the ijth grid cell would, on average, contribute significantly to the observed high rBC loading at Lulang.

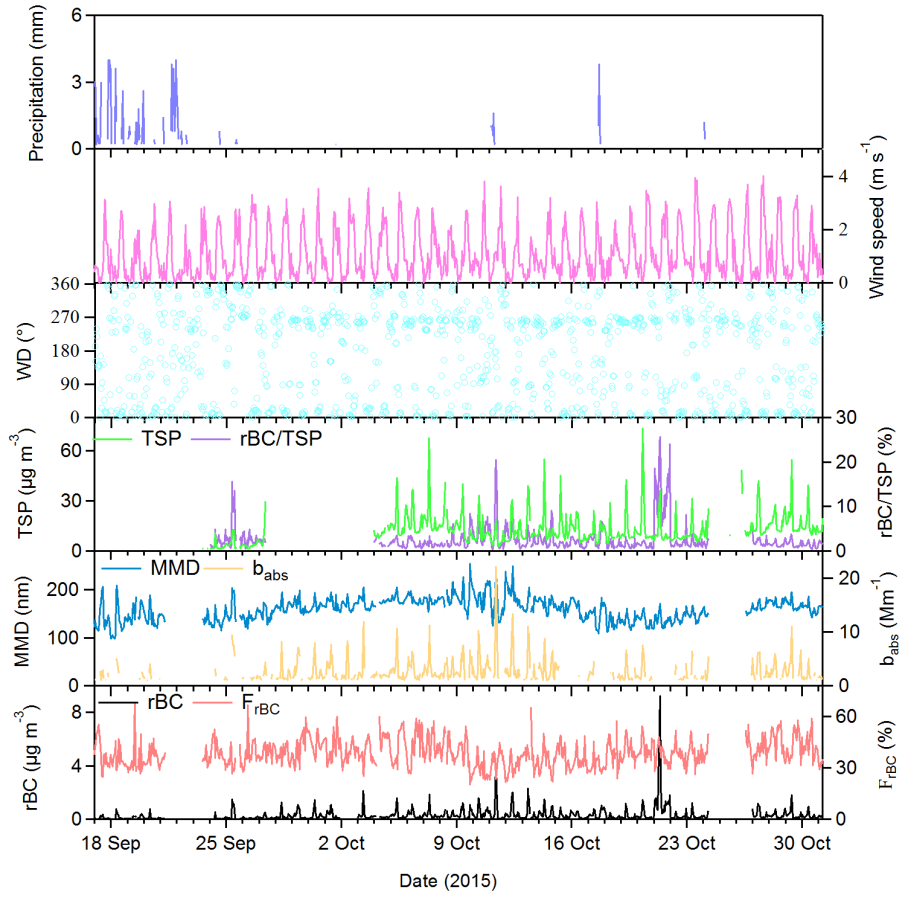

Figure 2. Time series plots of hourly averaged refractory black carbon (rBC) mass concentrations, number fraction of thickly coated rBC (F_{rBC}), mass median diameter of rBC particles (MMD), total suspended particulate matter (TSP), rBC/TSP, light absorption coefficient (b_{abs}), wind speed, wind direction (WD), and precipitation.

3 Results and discussion

3.1 Characteristics of surface rBC

3.1.1 rBC loadings

A time series plot of the hourly averaged mass concentrations of rBC and TSP during the entire campaign is shown in Fig. 2. The hourly average mass concentrations of rBC ranged from 0.002 to 9.23 μg m^{-3} with an arithmetic mean (±SD, standard deviation) of 0.31 ± 0.55 μg m^{-3}. A frequency distribution of the rBC mass concentrations (Fig. S5) shows that the rBC values formed a typical truncated normal distribution, with ∼60 % of all the data below 0.2 μg m^{-3}. However, the coefficient of variation (defined as SD/mean) for the rBC values was as high as 177 %. Furthermore, ∼25 % of the rBC mass loadings were above the 75th percentile value of 0.33 μg m^{-3}. These results simply show that the concentrations were quite variable, and at times large loadings of rBC occur at Lulang.

The total average mass concentration of TSP for the study was 12.65 ± 9.00 μg m^{-3}, which ranged from a minimum of 1.54 μg m^{-3} to a maximum of 73.40 μg m^{-3} (Fig. 2). The rBC particles accounted for 0.4–25.6 % of TSP mass and averaged 2.6 %. Figure S6 shows that the relationship between rBC and TSP followed two different patterns. On 21 October, the mass concentrations of rBC were highly correlated with the TSP mass concentrations ($r = 0.97$), but a weaker correlation ($r = 0.67$) was found for the other sampling days. Moreover, rBC accounted for 13.6 % of TSP mass on 21 October, but the contribution was considerably smaller (2.2 %) for other sampling days. As rBC is produced by combustion (Bond et al., 2013), these results indicate that combustion sources contributed significantly to TSP mass on 21 October, while particles from non-combustion related sources, such as secondary aerosols and soil dust, were relatively more abundant on the other sampling days.

Figure 1 shows the spatial distribution of BC mass concentrations at different high-altitude locations in the Himalayas and on the TP. Information for each study from which results

were taken is summarized in Table S1 in the Supplement. Although the sampling periods differed among the studies, BC generally exhibited larger loadings in the Himalayan foothills compared with those observed on the TP. On the other hand, the BC mass concentrations varied inversely with the altitude of the sampling sites ($r = -0.81$) (Fig. 1). The average rBC mass concentration at Lulang was higher than what has been measured in the interior or northern TP, but it was lower than at several locations on the southeastern TP and in the Himalayan foothills (Fig. 1). The differences in BC loadings among locations can be explained by several factors. First, the concentrations are undoubtedly affected by pollutant transport from upwind regions (e.g., South Asia), and this is influenced by the complex topography of the area. For example, Zhang et al. (2015) found that on annual average $\sim 50\,\%$ of the BC column burden of the Himalayas and TP was due to transport from South Asia ($\sim 33\,\%$ biomass and biofuel emissions and $\sim 17\,\%$ fossil fuel emissions). Second, the uncertainties caused by the inherent limitations of analytical methods themselves also help explain some of the differences in reported loadings. Indeed, previous studies have shown that the BC concentrations obtained from filter-based optical techniques (e.g., aethalometer) can be affected by the light-scattering artifacts (Virkkula et al., 2007), while laser-induced incandescence methods (e.g., SP2) can undersample small particles (Bond et al., 2013). Finally, there is still a lack of BC method intercomparisons, and there is some evidence that the differences among methods are greater for remote areas than urban ones. For instance, Wang et al. (2014) reported that a scaling factor of 2.5 was needed to adjust the eBC mass concentrations measured with an aethalometer to match SP2 measurements at a remote site on the northeastern TP, while the corresponding value at an urban site was 1.3. Moreover, filter-based EC measurements based on thermal–optical reflectance methods may be affected by the presence of carbonates (Li et al., 2017). In some areas of the TP, mineral dust particles, including carbonates, can contribute considerably to the aerosol populations due to the general lack of vegetative cover and long-range transport. Therefore, limitations such as those mentioned above make it difficult to establish scaling factors to reconcile the various BC measurements on the TP to a common standard, and direct comparisons of BC data obtained by different methods can be tenuous.

3.1.2 Diurnal variations

Figure 3a–c show the diurnal variations of the average rBC mass concentrations, PBL heights, and wind speeds during the campaign. The rBC mass concentrations decreased slightly after midnight to reach a low value of $0.16\,\mu g\,m^{-3}$ in the early morning, around 05:00 LT (local time – all time references below are given in LT); that was followed by a sharp increase at a rate of $0.35\,\mu g\,m^{-3}\,h^{-1}$ to a maximum value of $1.21\,\mu g\,m^{-3}$ around 09:00. The rBC loadings then decreased rapidly at $0.36\,\mu g\,m^{-3}\,h^{-1}$ and reached a diurnal minimum

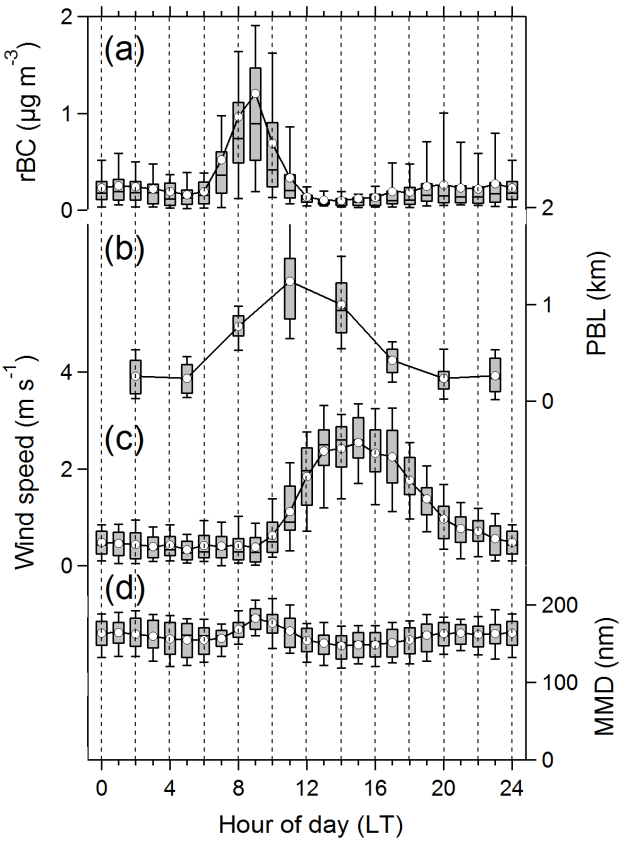

Figure 3. Diurnal variations of **(a)** refractory black carbon (rBC) mass concentrations, **(b)** planetary boundary layer (PBL) heights, **(c)** wind speeds, and **(d)** mass median diameters of the rBC particles (MMD). The lower and upper edges of the boxes denote the 25 and 75 % percentiles, respectively. The short black lines and white circles inside the boxes indicate the median and mean values, and the vertical bars ("whiskers") show the 10th and 90th percentiles. LT stands for local time.

of $0.10\,\mu g\,m^{-3}$ in the afternoon around 14:00. Thereafter, the rBC again increased gradually to a small peak of $0.26\,\mu g\,m^{-3}$ at night around 20:00. After that, the concentrations were relatively stable until 01:00.

Previous studies in urban areas have often shown a morning peak in BC caused by local rush hour traffic (e.g, Cao et al., 2009; Wang et al., 2016a). In contrast, slight morning enhancements in BC have been found at some sites on the TP, and those were attributed to local anthropogenic activities (e.g., Wang et al., 2014; M. Wang et al., 2016). In our study, a morning peak was observed at Lulang, but the rBC loadings' enhancements were as much as 6 times the minimum values. The morning peaks were consistent with the day-to-day activities of the local residents, especially cooking, indicating that there can be some contributions of rBC from local sources. However, local emissions alone may not explain such a large increase in concentrations in the morning. This can be assessed indirectly by comparing the morn-

ing peaks with the much smaller rBC enhancements in the evening around 19:00–20:00, which also were influenced by local cooking activities. Thus, the large morning peaks may have resulted from the combined effects of local activities and regional transport. As shown in Fig. 3a and b, the rapid morning increases in rBC were accompanied by deepening of the PBL, which suggests the possibility that regional transport had an important influence on rBC particles. Located to the southwest of Lulang, Bangladesh and the IGP are known to be strong sources of BC particles (Zhang et al., 2009). The PBL height is typically shallow and stable at night, and pollutants from the IGP and Bangladesh tend to be confined near the surface at that time. After sunrise, as the PBL starts to deepen, strengthening thermals lift and eventually break up the nighttime inversion. These changes in the atmosphere provide conditions that could support the transport of pollutants to the southeastern TP.

This explanation concerning the effects of transport is further supported by the analysis of true color images of haze clouds retrieved by MODIS on the Terra satellite (Fig. S7). That satellite passed over the study region at ∼ 10:30, and even though only several sampling days (20–23 October) were selected for inclusion in Fig. S7, most days exhibited similar patterns. The true color images reveal obvious pollution bands along the IGP and Bangladesh that piled up on the southern margin of the TP. The prevailing wind direction around the southeastern margin of the TP was southerly (Fig. S7), and therefore, the aerosols in the pollution bands were subject to transport along the valley of the Yarlung Tsangpo River to our sampling site. Indeed, this pathway has been considered a "leaking wall" for pollutant transport to the southeastern TP (Cao et al., 2010).

The decreasing trend in rBC loadings in the late morning at Lulang is consistent with the continued deepening of the PBL (Fig. 3b) and the strengthening winds from the northeast (see Figs. 2 and 3c). Those meteorological conditions also can explain the daily minima in the rBC loadings in the afternoon because they cause the dilution and dispersal of the ambient aerosols, including rBC. The slight enhancement of rBC at night can be attributed to shallow PBLs and low winds in addition to increased local rBC anthropogenic emissions from daily activities, such as cooking and heating. It should be noted that even though the average rBC concentration from 08:00 to 10:00 on 21 October was ∼ 8 times higher than the average value for other sampling days, the diurnal pattern of 21 October was similar to that seen on other days (Fig. S8a). Indeed, the rBC diurnal loading pattern did not appear to be different on this high rBC concentration day (Fig. S8b and c). Over short timescales, such as the length of our study, one can assume that the local emission sources are relatively stable. Based on the 3-day backward trajectory analysis, sudden high rBC loadings such as those on the morning on 21 October may be explained by the slow passage of air over Guwahati in northeastern India (Fig. S9). Large numbers of rBC particles likely accumulated in the air as it slowly passed over this polluted region, and it was those particles that were eventually transported to Lulang.

3.2 Meteorological effects on rBC concentrations

Wet deposition is the major mechanism by which BC aerosol is removed from the atmosphere (Bond et al., 2013). During the rain events at Lulang, the hourly precipitation varied from 0.2 to 4.0 mm (Fig. 2). The total sum of precipitation during the campaign was 104.8 mm. Rain events occurred in ∼ 30 % of the sampling period, and ∼ 70 % of the rain occurred in September due to the influx of moist warm air from the Indian and Pacific oceans (Kang et al., 2002). The average mass concentration of rBC during rainy days ($0.25 \pm 0.13\,\mu g\,m^{-3}$) was ∼ 45 % lower than on non-rainy days ($0.36 \pm 0.38\,\mu g\,m^{-3}$). Figure S10 shows the impact of daily precipitation on rBC loadings; that is, the rBC mass concentrations were negatively correlated with precipitation amount ($r = -0.51$). In the classification scheme for daily precipitation issued by the China Meteorological Administration (GB/T 28592-2012), light, moderate, and heavy rain is defined as precipitation with ranges of 0.1–9.9, 10.0–24.9, and 25.0–49.9 mm within 24 h, respectively. When the daily precipitation was less than 10 mm, the rBC loadings had large fluctuations, ranging from 0.06 to $0.45\,\mu g\,m^{-3}$. However, when the daily precipitation was higher than 10 mm, the rBC values were $< 0.14\,\mu g\,m^{-3}$, suggesting that rBC particles are removed more efficiently by moderate or strong rain compared with light rain. A t test for the rBC concentrations during light and strong rains showed that there was a statistically significant difference between them at a probability for chance occurrence of $p < 0.01$.

Wind speed and wind direction play crucial roles in the dilution and dispersion of pollutants (Fast et al., 2007). Figure 4a shows the wind speeds and directions during the study. Overall, the prevailing surface wind directions were westerly and northerly, and these sectors combined accounted for ∼ 70 % of the total wind frequencies. The average wind speed was $1.07 \pm 0.93\,m\,s^{-1}$, and the higher wind speeds were most often associated with northerly flow. To investigate the potential for the horizontal advection of rBC, we examined the relationships between rBC loadings and wind speed and wind direction using a bivariate polar plot (Fig. 4b). When the wind speed exceeded $1\,m\,s^{-1}$, large rBC loadings were associated with airflow from the southeast. This is the compass sector that captures transport from Yarlung Tsangpo River valley, which as noted above can bring pollutants to our site from the IGP and Bangladesh (Cao et al., 2010; S. Zhao et al., 2017). High rBC mass concentrations also occurred under static conditions or low winds ($< 1\,m\,s^{-1}$), which typically promote the accumulation of locally generated pollutants near the Earth's surface. In contrast, low levels of rBC were observed when the winds were from the north–northwest. This is likely because upwind regions in those directions contained few rBC sources.

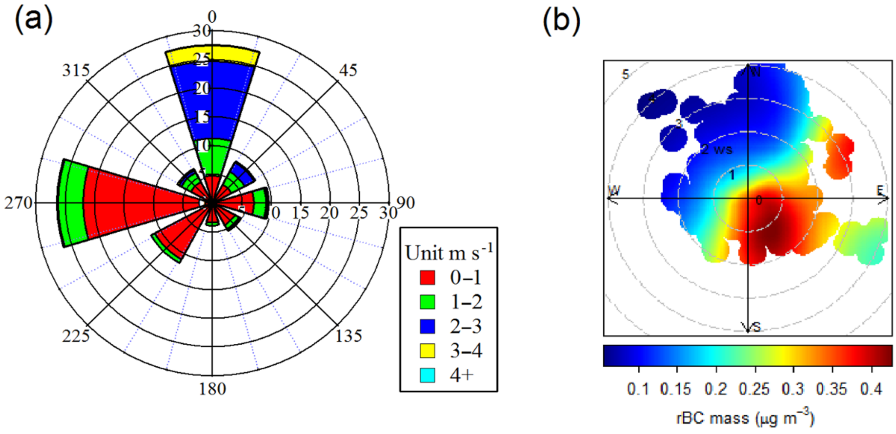

Figure 4. **(a)** Wind rose plot and **(b)** bivariate polar plot for the refractory black carbon (rBC) mass concentrations based on hourly data.

Therefore, strong winds from the north–northwest sectors would tend to dissipate the rBC particles.

To evaluate the surface transport of rBC to Lulang from the south (arbitrarily designated as positive, from outside the TP, e.g., IGP and Bangladesh) and north (negative, from the interior of the TP), surface transport intensities were calculated from Eq. (1) based on the observed rBC mass concentrations, wind speed, and wind direction at the sampling site. The estimated overall net surface transport of rBC was $+0.05 \pm 0.29\,\mu g\,s^{-1}$, indicating greater transport of rBC from outside of the TP than from the interior of it. The large coefficient of variation (580 %) of the surface transport intensity reflects strong fluctuations in transport, and at least two factors likely influenced the transport processes. First, the surface fluxes were more than likely strongly affected by the prevailing winds. Figure 5 shows the variations in the hourly averaged surface transport intensity of rBC and the corresponding wind vectors ($m\,s^{-1}$). In general, the rBC transport intensities exhibited a clear "saw-toothed" pattern, with changes in the influx (positive) and outflux (negative) patterns corresponding to shifts in wind direction (Fig. 5a). Second, differences in the emission intensities for pollutants in the upwind areas are another factor that likely affected the transport of rBC. For example, the average influx intensity ($+0.18 \pm 0.27\,\mu g\,s^{-1}\,m^{-2}$) for rBC, which includes transport from IGP and Bangladesh, was twofold stronger than the efflux intensity ($-0.09 \pm 0.24\,\mu g\,s^{-1}\,m^{-2}$) (Fig. 5b).

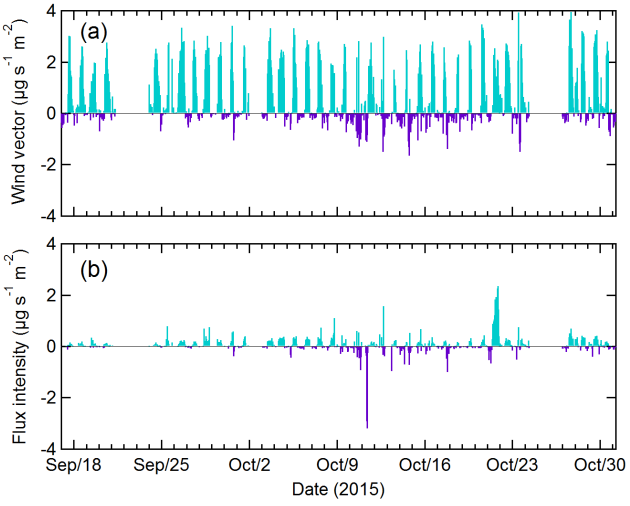

Figure 5. Time series plots of **(a)** wind vector ($= \frac{1}{n}\sum_{j=1}^{n} WS_j \times \cos\theta_j$) and (b) surface transport intensity for refractory black carbon (rBC) based on the hourly averaged data at the Lulang site. Positive values indicate the transport direction of rBC from south to north (i.e., from the Indo-Gangetic Plain and Bangladesh to Lulang) and the negative values represent the transport direction of rBC from north to south (i.e., from the interior of the Tibetan Plateau) to Lulang.

3.3 Effects of regional transport

Figure 6a shows the three cluster mean trajectories that were constructed from the individual 3-day backward trajectories for the campaign. For discussion purposes, we arbitrarily defined a trajectory as "polluted" if it corresponded to an rBC concentration higher than the 75th percentile value of $0.33\,\mu g\,m^{-3}$; otherwise it was classified as a "clean" trajectory. The average rBC mass concentrations for the three clusters and the polluted trajectories are summarized in Table 1. The air masses grouped into Cluster no. 1 originated from north India and passed through central Nepal and the southern TP before arriving at Lulang. The average rBC mass concentration for Cluster no. 1 was $0.37 \pm 0.71\,\mu g\,m^{-3}$. Of all 887 backward trajectories included in the analysis, ~47 % were allocated to Cluster no. 1, and ~29 % of those were considered polluted. The average rBC mass concentration for these polluted trajectories was $0.95\,\mu g\,m^{-3}$. The air masses grouped into Cluster no. 1 were responsible for many of the

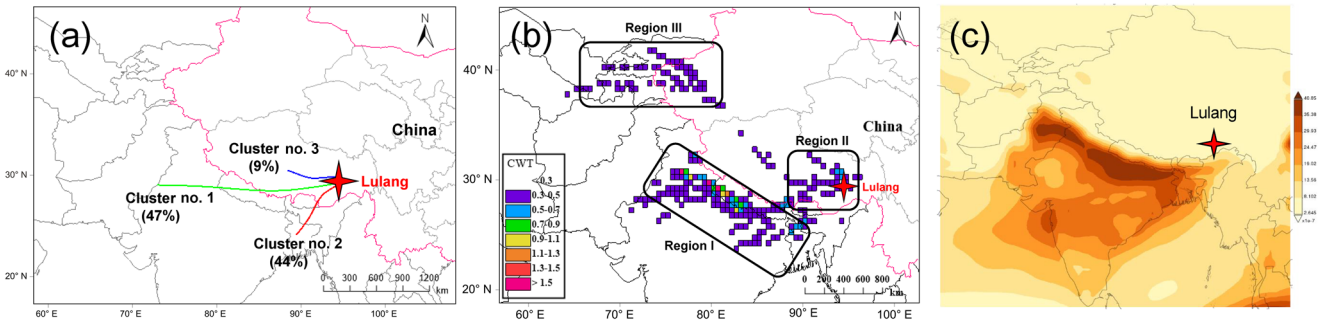

Figure 6. Maps of **(a)** the mean trajectory clusters, **(b)** the concentration-weighted trajectories (CWT, $\mu g\,m^{-3}$) for refractory black carbon mass concentrations, and **(c)** the reconstructed black carbon column mass densities ($kg\,m^{-2}$) during the campaign.

Table 1. Trajectory clusters and mean refractory black carbon (rBC) concentration for each cluster.

Cluster	All trajectories			Polluted rBC trajectories[a]		
	Number	Mean	SD[b]	Number	Mean	SD[b]
no. 1	421	0.37	0.71	120	0.95	1.14
no. 2	390	0.24	0.36	81	0.75	0.52
no. 3	76	0.32	0.31	23	0.72	0.29
All	887	0.31	0.55	224	0.86	0.90

[a] Trajectories associated with rBC concentration > 0.33 $\mu g\,m^{-3}$ (75th percentile value).
[b] SD represents standard deviation.

high rBC loadings at the receptor site. The air masses associated with Cluster no. 2 originated from central Bangladesh and then moved across northeastern India and to the southeast of Tibet before arriving at Lulang. The average rBC mass concentration for Cluster no. 2 was $0.24 \pm 0.36\,\mu g\,m^{-3}$. The percentage of the trajectories assigned to this cluster was ~ 44 %, and ~ 20 % of those were regarded as polluted. The average mass concentration of the polluted trajectories in Cluster no. 2 was $0.75\,\mu g\,m^{-3}$. The air masses in Cluster no. 3 originated over central Tibet, and the average rBC mass concentration for this cluster ($0.32 \pm 0.31\,\mu g\,m^{-3}$) was similar to that for Cluster no. 1. Although the percent contribution from this cluster was ~ 9 % of all trajectories, ~ 30 % of the trajectories in Cluster no. 3 were classified as polluted, and they had a mean value of $0.72\,\mu g\,m^{-3}$. This implies some contributions of rBC from internal Tibetan sources.

A CWT model was used to better identify the locations of the potential source areas that provided rBC to Lulang, and a map of the CWT results for the campaign is shown in Fig. 6b. There were three main source regions contributing to the rBC pollution at Lulang. Region I was mainly composed of areas along the southern border of the Himalayan foothills, IGP, and north Bangladesh. This region had the highest CWT values, indicating that this area had the greatest probability for causing the high rBC loadings at Lulang, and it is also worth noting that there are high BC column mass densities in this area (Fig. 6c). In contrast, moderate CWT values were found for areas to the west of Lulang and adjoining regions (Region II), suggesting local anthropogenic activities in the interior of the TP also contributed to the rBC loadings at Lulang. Several cities, including Lhasa, Gongbu Jiang, and Linzhi, are located ~ 60–350 km to the west of Lulang, and these are possible sources of anthropogenic materials. Although the population is sparse in the areas surrounding Lulang, biofuels, especially wood and yak dung, are the main energy sources for local residents (Ping et al., 2011). Domestic heating and cooking using these fuels typically produces large quantities of rBC particles, and therefore, these sources probably affected the sampling site. Region II evidently had lesser effects on the rBC loadings compared with the Region I because the CWT values for Region II were lower. It is worth noting that even though Region III extended to the southwest of Sinkiang Province, China, and several central Asian countries that emit substantial quantities of BC, this region had only minor impacts on the rBC because the air masses from Region III composed less than ~ 1 % of the total trajectories.

3.4 Microphysical properties

3.4.1 Size distributions of rBC

Figure S1 shows that rBC core size distribution was well represented by a mono-modal log-normal fit. This is consistent with the size distributions constructed from previous SP2-based observations made across the globe, including urban, rural, and remote areas (e.g., Schwarz et al., 2008; Liu et al., 2010; McMeeking et al., 2011; Huang et al., 2012; Wang et al., 2014). As shown in Fig. 2, the hourly averaged mass median diameters (MMDs – the VED at the peak of the mass distribution) varied broadly from 98 to 255 nm during the study, and the average was 160 ± 23 nm. The rBC MMDs exhibited diurnal patterns similar to the rBC mass concentrations; that is, they peaked in the morning around 09:00 (~ 183 nm), fell to a minimum in the afternoon around 14:00 (~ 147 nm), then rose again in the evening, and finally stabilized at night (~ 163 nm) (Fig. 3d).

Although size-segregated filter-based measurements made with cascade impactors provide information on the aerodynamic diameters of BC particles, they measure both the BC cores and any coatings on the particles. In contrast, the SP2 measures the rBC core size alone. Consequently, we only compared our results with SP2 observations made in previous studies. Because of the different rBC densities assumed in the various studies, we normalized them to the same density of 1.8 g cm^{-3} to facilitate direct comparisons. The average rBC MMD at Lulang fell into the lower range reported in previous SP2 studies ($\sim$ 155–240 nm; Huang et al., 2012, and references therein), and it was lower than some results reported for remote areas, such as 181 nm at Qinghai Lake, northeastern TP (Wang et al., 2014), 194 nm at the Pallas Global Atmosphere Watch station, Finnish Arctic (Raatikainen et al., 2015), and 220–240 nm at the high alpine research station Jungfraujoch, Switzerland (Liu et al., 2010).

The variations in rBC MMDs among sites were likely related to the following factors. First, the various emission sources produce rBC particles of different sizes. For example, Sahu et al. (2012) observed larger average rBC MMDs in biomass burning plumes (193 nm) compared with fossil fuel plumes (175 nm). Wang et al. (2016b) reported a higher average rBC MMD for coal burning (215 nm) compared with particles from a traffic source (189 nm). Second, transport histories matter because aging of the particles can affect the size distributions of rBC. Take the cluster analysis as an example: the average rBC MMD was the largest (184 ± 17 nm) when the polluted air masses originated from central Bangladesh (Cluster no. 2). In contrast, smaller rBC MMDs were found when the polluted air masses came from north India (Cluster no. 1, 173 ± 26 nm) or the central TP (Cluster no. 3, 177 ± 19 nm). These air masses originated from different sources regions, and they may have had different rBC sizes initially; but the rBC core sizes also may have changed during transport through coagulation. It should be noted that a t test for the rBC MMDs from different clusters showed that there was a statistically significant difference between Cluster no. 1 and no. 2 ($p < 0.01$) but no significant difference between Cluster no. 2 and no. 3 ($p = 0.09$).

Finally, wet deposition may exert a significant effect on the rBC size distributions. This can be seen in Fig. 7, which presents a comparison of the frequency distributions of rBC MMDs during rainy and non-rainy sampling days. The rBC MMDs varied from 112 to 255 nm with an average of 164 ± 21 nm for the non-rainy days, and about 50 % of the MMDs were within the range of 150–175 nm. In contrast, the rBC MMDs for rainy days shifted toward smaller sizes, varying from 98 to 230 nm and averaging 145 ± 25 nm. About 40 % of the MMDs for the rainy day samples were in the range of 125–145 nm. We note that the sizes of the particles on rainy days may be representative of local sources because rain also fell over South Asia, and therefore, there was little long-range transport of rBC to Lulang under those conditions. Compared with non-rainy days, the smaller rBC on rainy days can be explained by the absence of long-range transport and by the preferential wet scavenging of larger rBC cores (Taylor et al., 2014).

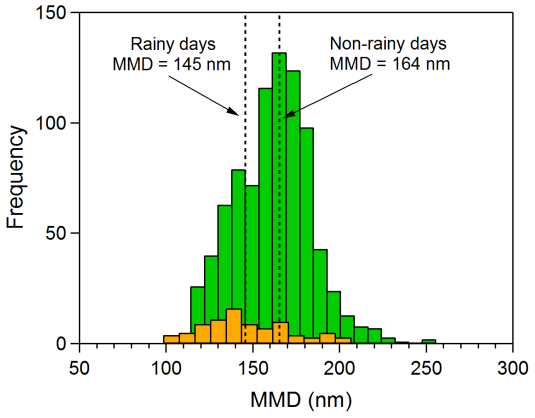

Figure 7. Frequency distributions of mass median diameters (MMDs) for rainy and non-rainy sampling days. The vertical dashed lines denote the average MMDs for those two types of days.

3.4.2 Evolution of rBC mixing state

The average F_{rBC} was 39 ± 8 % (range of 20–68 %, Fig. 2) during the entire campaign, which is lower than what has been reported for Qinghai Lake (59 %, Wang et al., 2015a), where a similar method was used to measure the internal mixing of rBC. Air masses in Cluster no. 2 showed the highest internal mixing of rBC particles (40 %), followed by Cluster no. 1 (38 %) and Cluster no. 3 (34 %). The low percentages of internal mixing for rBC particles in these three clusters indicate a relatively low level of particle aging. This implies that freshly emitted local rBC particles were part of the sample population. Figure 8a shows that the diurnal cycle of F_{rBC} at Lulang typically exhibited "two peaks and two valleys". The percentage of internally mixed rBC reached a peak value of 45 % in the morning around 07:00–08:00, followed by a decreasing trend to a low value of 35 % around 10:00. The internally mixed rBC then increased to a secondary peak value of 44 % in the afternoon around 14:00 and again slowly decreased to a minimum of 33 % around 01:00.

The variations in percentages of internally mixed rBC in the morning further provide evidence for the combined effects of local activities and regional transport on the rBC aerosol. That is, the enhancement of internally mixed rBC around 07:00–08:00 can be attributed to rBC aging, which indicates impacts from regional transport. The decreasing trend of F_{rBC} around 09:00–10:00 was likely due to an increase in fresh rBC particles emitted by local anthropogenic activities, even though the local population was small. As the day progressed from 10:00 to 19:00, F_{rBC} varied with O_3 mixing ratios (Fig. 8a), suggesting a possible effect of oxidants on the internal mixing of rBC. It can be seen in Fig. 8b that F_{rBC} was

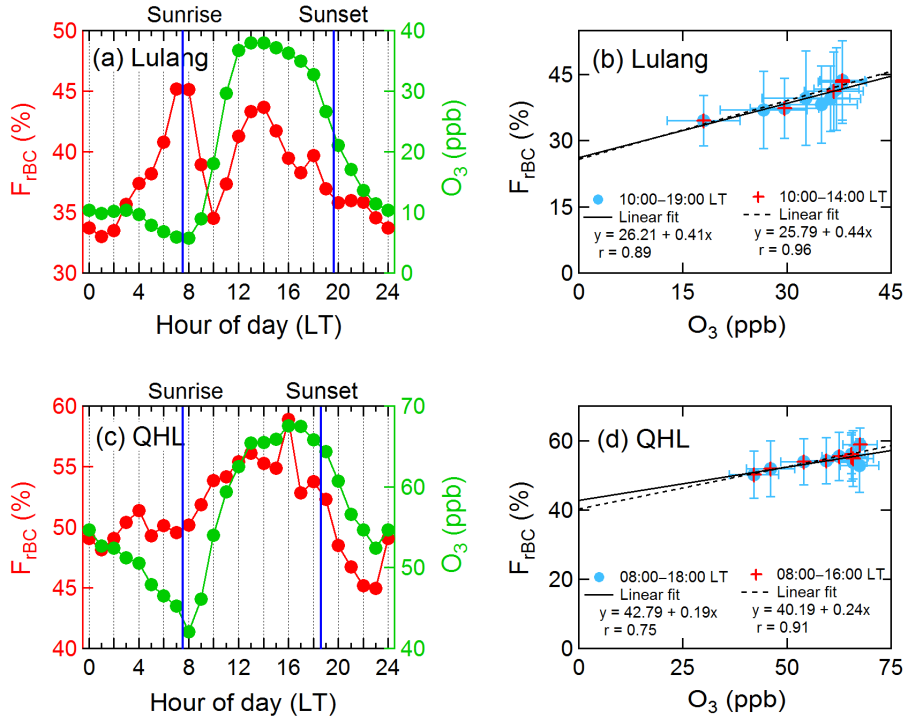

Figure 8. (a, c) Diurnal variations of the hourly averaged number fraction of thickly coated refractory black carbon particles (F_{rBC}) and O_3 mixing ratios at Lulang and Qinghai Lake (QHL) and **(b, d)** linear regressions between F_{rBC} and O_3 at these two sites.

positively correlated with the O_3 mixing ratio ($r = 0.89$), indicating that more internal mixing for rBC particles occurred under more oxidizing conditions. Further, the observed increasing trend for internally mixed rBC from 10:00 to 14:00 can be explained by the mixing of rBC particles with secondary aerosols (e.g., non-refractory inorganic and organic compounds) that resulted from enhanced photochemical oxidation due to the daily cycle in insolation.

To further investigate the effects of photochemical oxidation on the rBC mixing state, we compared the diurnal variations of internal mixing for rBC particles at Lulang with observations made at Qinghai Lake, a site in the northeastern TP, where studies were conducted in October 2011 (Fig. 8c). The rBC and O_3 at Qinghai Lake were measured with the same type of SP2 as in this study and an ultraviolet photometer, respectively. Detailed descriptions of the Qinghai Lake study may be found in Wang et al. (2014, 2015b). As shown in Fig. 8c, only one F_{rBC} peak was observed at Qinghai Lake in the afternoon between 12:00 and 17:00, which was different from what we observed at Lulang. This difference can be explained by the fact that rBC in the early morning at Qinghai Lake was not affected by long-range transport, owing to the topography of the region (Wang et al., 2014). Even so, similar to Lulang, the F_{rBC} during the daytime (08:00–18:00) at Qinghai Lake was positively correlated with the O_3 mixing ratio ($r = 0.75$, Fig. 8d), and these results are additional evidence that photochemical oxidation is involved in the formation of the coatings on rBC particles from the TP. Moreover, the variations in F_{rBC} during the daytime at Lulang also co-varied with the PBL height, indicating that aged rBC particles may have been transported from aloft to the surface.

3.5 rBC optical properties

The average b_{abs} at $\lambda = 870$ nm for the campaign was $2.9 \pm 2.4\ Mm^{-1}$ (Fig. 2). Some organic materials (also called brown carbon) can cause significant light absorption, but those effects are mainly at short wavelengths (e.g., $\lambda = 370$ nm), and they have nearly no absorption in the near-infrared spectral region (e.g., $\lambda = 870$ nm) (Laskin et al., 2015). Consequently, it is reasonable to calculate the mass absorption cross section of rBC (MAC_{rBC}, $m^2\ g^{-1}$), which describes the degree of light absorption per unit mass of rBC, by dividing the b_{abs} measured with the PAX_{870} by the mass concentration of rBC detected with the SP2 ($MAC_{rBC} = b_{abs}/rBC$). Figure 9 shows that the MAC_{rBC} frequency distributions were mono-modal log-normal for all samples from the campaign and for the data stratified by the three trajectory clusters. The peak in the frequency MAC_{rBC} distribution for the entire campaign was $7.6\ m^2\ g^{-1}$, and there were slightly higher values for Cluster no. 1 ($8.0\ m^2\ g^{-1}$) and Cluster no. 2 ($7.8\ m^2\ g^{-1}$) compared with Cluster no. 3 ($7.5\ m^2\ g^{-1}$).

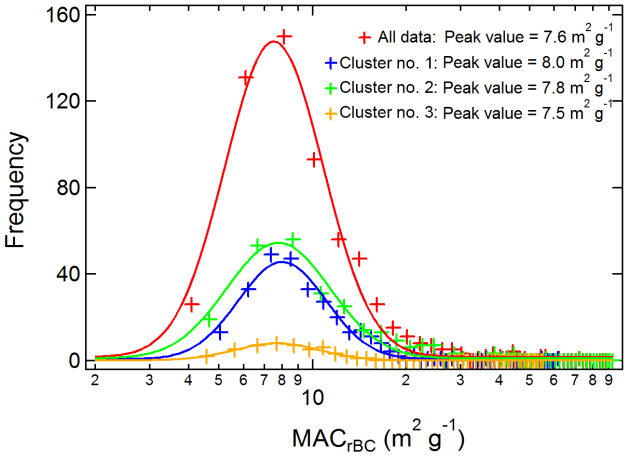

Figure 9. Frequency distributions of the mass absorption cross sections of refractory black carbon (MAC_{rBC}) for the campaign and for air masses defined by trajectory cluster.

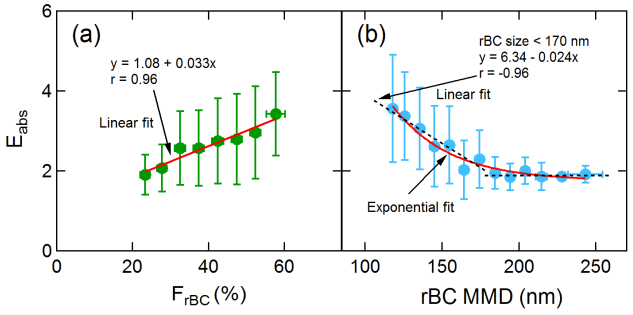

Figure 10. Absorption enhancement (E_{abs}) versus **(a)** the number fraction of thickly coated refractory black carbon (F_{rBC}) and **(b)** the mass median diameter (MMD) of rBC during the campaign. The error bars correspond to the standard deviations of E_{abs}, F_{rBC}, and MMD.

Absorption enhancements for the rBC ($E_{abs} = MAC_{rBC}/MAC_{rBC,uncoated}$) were calculated to further characterize the rBC particles' optical properties. As the SP2 only determines the rBC core size, the hourly averaged MMDs for the rBC were input into the Mie model to calculate the MAC_{rBC} of uncoated rBC particles ($MAC_{rBC,uncoated}$), assuming that the uncoated rBC particles were spherical and homogeneous. A more detailed description of the Mie algorithms may be found in Bohren and Huffman (2008). For these calculations, the refractive index of 1.85–0.71i at $\lambda = 550$ nm suggested by Bond and Bergstrom (2006) was first used in the Mie model to estimate the $MAC_{rBC,uncoated}$. Those values were then converted to the $MAC_{rBC,uncoated}$ at $\lambda = 870$ nm based on an rBC absorption Ångström exponent of 1.0 (Moosmüller et al., 2011). Finally, the average rBC absorption enhancement was calculated by comparing the MAC_{rBC} at $\lambda = 870$ nm for rBC with and without coatings. As shown in Fig. 9, there were several anomalously large MAC_{rBC} values that were likely caused by the uncertainties associated with extremely low b_{abs} and rBC mass concentrations. To avoid spurious results such as these, only MAC_{rBC} values in the lower 90th percentile of all data were used to calculate the E_{abs}. As shown in Fig. S11, the E_{abs} values generally followed a mono-modal log-normal distribution with a peak value of 1.9, which is an indication that the light absorption of coated rBC particles was significantly greater than that of uncoated ones.

To investigate the potential impacts of rBC size and mixing state on light absorption, the E_{abs} values were plotted against the F_{rBC} values and MMDs (Fig. 10). As shown in Fig. 10a, the E_{abs} was strongly positive correlated with the F_{rBC} ($r = 0.96$), and this supports our conclusion that there was an enhancement of light absorption by internally mixed – that is, coated – rBC particles. The slope of the regression line was 0.03 $\%^{-1}$, which may be considered a rough estimate of the effects of the coatings on light absorption. This means that if the fraction of thickly coated rBC particles increased by 1 %, the rBC particles would absorb 3 % more light. If the results of the linear regression shown in Fig. 10a are extrapolated to a condition in which rBC is completely uncoated (that is, F_{rBC} or $x = 0$ %), the E_{abs} would be 1.1, which is close to the theoretical value of 1.0 for uncoated rBC. At the other extreme, if all rBC particles were internally mixed (F_{rBC} or $x = 100$ %), the E_{abs} would be as high as 4.4, which appears physically implausible. This result is confined to a narrow range of conditions, however, that is, small rBC core diameters with the thick coatings (Bond et al., 2006). Moreover, it is noteworthy that several studies have shown nonlinear relationships between E_{abs} and the internal mixing of rBC (e.g., Zhang et al., 2016; Liu et al., 2015). In those cases, the E_{abs} tended to be stable over a large range of coating thicknesses. If that were the case in our study, the E_{abs} would be lower than the calculated value of 4.4.

As shown in Fig. 10b, the E_{abs} was nonlinearly related to the MMDs of the rBC. When rBC MMD < 170 nm, the E_{abs} varied inversely with rBC core size, indicating that smaller rBC particles potentially have a stronger ability to amplify light absorption than large ones. This can be explained by the greater tendency of small rBC particles to form coatings than the large ones, which is due to the well-known relationship between particle surface area and volume (see the positive correlation between F_{rBC} and MMDs in Fig. S12). The variations in E_{abs} were relatively constant for rBC MMD > 170 nm. When coatings form by condensation, a 1 diameter^{-1} dependence would apply to the condensation rate. Thus, larger rBC cores have a smaller degree of internal mixing and weaker absorption amplification than smaller cores on the one hand, but on the other hand, larger rBC core size also would decrease the $MAC_{rBC,uncoated}$ according to the Mie model (see the relationship between $MAC_{rBC,uncoated}$ and MMD in Fig. S12). Eventually, the decrease in light ab-

sorbing ability for the measured ambient rBC (that is, the MAC_{rBC}) and for the assumed uncoated rBC particles (that is, $MAC_{rBC,uncoated}$) would cancel out, causing a constant value for E_{abs}. Indeed, Bond et al. (2006) reported that the amplification was nearly constant for rBC cores $> \sim 150$ nm.

4 Conclusions

The mass concentrations, size distributions, mixing state, and optical properties of rBC aerosol were studied at Lulang on the southeastern TP, China. The mass concentration of rBC, averaged over the entire campaign, was $0.31 \pm 0.55\,\mu g\,m^{-3}$, and the rBC particles accounted for 2.6 % of TSP mass. A clear diurnal pattern in rBC mass concentrations was observed: high values occurred in the early morning due to the combined effects of local anthropogenic activities and regional transport, while low values in the afternoon were ascribed to the dispersion of the rBC due to deepening of the PBL and higher wind speeds. The relationship observed between rainfall and rBC indicated that rBC particles were more efficiently removed by moderate and heavy precipitation (> 10 mm) than by light rain. A bivariate polar plot showed that high rBC loadings were associated with strong winds from the southeast or static wind conditions. The estimated overall net surface transport intensity of rBC was $+0.05 \pm 0.29\,\mu g\,s^{-1}\,m^{-2}$. Those calculations showed that more rBC was brought to the site from outside the TP than from the interior of the TP. Moreover, air mass trajectory clusters and a concentration-weighted trajectory model indicated that sources in north India were the most important influences on rBC at Lulang, but local contributions were not negligible.

The rBC VEDs showed approximately mono-modal log-normal distributions. The hourly average rBC MMD was 160 ± 23 nm, and the MMDs varied among air parcels. The MMDs shifted toward smaller sizes (145 nm) on rainy days compared with non-rainy days (164 nm). The average F_{rBC} for the study was 39 ± 8 %, suggesting uncoated or thinly coated rBC particles composed the bulk of the rBC population. Two peaks in F_{rBC} were observed: one was in the morning, which was attributed to atmospheric aging processes; the other was in the afternoon, which was explained by enhancements caused by photochemical oxidation and the mixing aged rBC particles from aloft into the surface. A strong correlation between F_{rBC} and O_3 was found during the daytime at Lulang (10:00–19:00), indicating that the photochemical oxidation played an important role in the internal mixing of rBC with other materials. A similar relationship was found for samples from near Qinghai Lake in the northeastern TP.

The total average b_{abs} (at $\lambda = 870$ nm) for the study was $2.9 \pm 2.4\,Mm^{-1}$. The MAC_{rBC} values showed a mono-modal log-normal distribution with a peak value of $7.6\,m^2\,g^{-1}$. Slightly higher MAC_{rBC} values were found for air masses from north India ($8.0\,m^2\,g^{-1}$) and central Bangladesh ($7.8\,m^2\,g^{-1}$) compared with air transported from central Tibet ($7.5\,m^2\,g^{-1}$). By dividing the observed MAC_{rBC} measured with the SP2 and PAX_{870} by the $MAC_{rBC,uncoated}$ calculated from the Mie model, the average E_{abs} was estimated to be 1.9. This suggests that the light absorption by coated rBC particles was significantly amplified compared with uncoated ones. Furthermore, the E_{abs} was positively correlated with F_{rBC}, indicating an enhancement of light absorption by internally mixed rBC particles. The E_{abs} showed a negative correlation with the rBC MMDs for the particle cores < 170 nm, but it was nearly constant for larger rBC cores. We should note that the sources, transport, and radiative effects of the rBC as well as atmospheric conditions likely vary in complex ways with season, and therefore the results from our study (in autumn) are not necessarily representative of other times of the year. Indeed, additional studies need to be conducted to determine how the rBC aerosol at our site and others changes with season.

Data availability. All data described in this study are available upon request from the corresponding authors.

The Supplement related to this article is available online at https://doi.org/10.5194/acp-18-4639-2018-supplement.

Competing interests. The authors declare that they have no conflict of interest.

Special issue statement. This article is part of the special issue "Atmospheric pollution in the Himalayan foothills: The SusKat–ABC international air pollution measurement campaign". It is not associated with a conference.

Acknowledgements. This work was supported by the National Natural Science Foundation of China (41230641, 41503118, 41625015, and 41661144020). The authors are grateful to the Southeast Tibet Integrated Observation and Research Station for the Alpine Environment, Chinese Academy of Sciences, for their assistance with field sampling.

Edited by: Ernest Weingartner
Reviewed by: four anonymous referees

References

Babu, S. S., Chaubey, J. P., Moorthy, K. K., Gogoi, M. M., Kompalli, S. K., Sreekanth, V., Bagare, S. P., Bhatt, B. C., Gaur, V. K., Prabhu, T. P., and Singh, N. S.: High altitude (similar to 4520 m amsl) measurements of black carbon aerosols over western trans-Himalayas: Seasonal heterogeneity and source apportionment, J. Geophys. Res., 116, D24201, https://doi.org/10.1029/2011JD016722, 2011.

Bohren, C. F. and Huffman, D. R.: Absorption and scattering of light by small particles, John Wiley & Sons, New York, 2008.

Bond, T. C. and Bergstrom, R. W.: Light absorption by carbonaceous particles: an investigative review, Aerosol Sci. Tech., 40, 27–67, https://doi.org/10.1080/02786820500421521, 2006.

Bond, T. C., Habib, G., and Bergstrom, R. W.: Limitations in the enhancement of visible light absorption due to mixing state, J. Geophys. Res., 111, D20211, https://doi.org/10.1029/2006JD007315, 2006.

Bond, T. C., Doherty, S. J., Fahey, D. W., Forster, P. M., Berntsen, T., DeAngelo, B. J., Flanner, M. G., Ghan, S., Karcher, B., Koch, D., Kinne, S., Kondo, Y., Quinn, P. K., Sarofim, M. C., Schultz, M. G., Schulz, M., Venkataraman, C., Zhang, H., Zhang, S., Bellouin, N., Guttikunda, S. K., Hopke, P. K., Jacobson, M. Z., Kaiser, J. W., Klimont, Z., Lohmann, U., Schwarz, J. P., Shindell, D., Storelvmo, T., Warren, S. G., and Zender, C. S.: Bounding the role of black carbon in the climate system: A scientific assessment, J. Geophys. Res.-Atmos., 118, 5380–5552, https://doi.org/10.1002/jgrd.50171, 2013.

Cao, J.: The importance of aerosols in the earth system: science and engineering perspectives, Aerosol Sci. Eng., 1, 1–6, https://doi.org/10.1007/s41810-017-0005-1, 2017.

Cao, J.-J., Zhu, C.-S., Chow, J. C., Watson, J. G., Han, Y.-M., Wang, G.-H., Shen, Z.-X., and An, Z.-S.: Black carbon relationships with emissions and meteorology in Xi'an, China, Atmos. Res., 94, 194–202, https://doi.org/10.1016/j.atmosres.2009.05.009, 2009.

Cao, J. J., Tie, X. X., Xu, B. Q., Zhao, Z. Z., Zhu, C. S., Li, G. H., and Liu, S. X.: Measuring and modeling black carbon (BC) contamination in the SE Tibetan Plateau, J. Atmos. Chem., 67, 45–60, https://doi.org/10.1007/s10874-011-9202-5, 2010.

Chen, P., Kang, S., Bai, J., Sillanpää, M., and Li, C.: Yak dung combustion aerosols in the Tibetan Plateau: Chemical characteristics and influence on the local atmospheric environment, Atmos. Res., 156, 58–66, 2015.

Cong, Z., Kang, S., Kawamura, K., Liu, B., Wan, X., Wang, Z., Gao, S., and Fu, P.: Carbonaceous aerosols on the south edge of the Tibetan Plateau: concentrations, seasonality and sources, Atmos. Chem. Phys., 15, 1573–1584, https://doi.org/10.5194/acp-15-1573-2015, 2015.

Draxler, R. R. and Rolph, G. D.: HYSPLIT (HYbrid Single-Particle Lagrangian Integrated Trajectory), Silver Spring, MD, Model access via NOAA ARL READY Website: http://www.arl.noaa.gov/ready/hysplit4.htmlNOAAAirResourcesLaboratory (last access: March 2017), 2003.

Dyurgerov, M. B., and Meier, M. F.: Twentieth century climate change: Evidence from small glaciers, P. Natl. Acad. Sci. USA, 97, 1406–1411, https://doi.org/10.1073/pnas.97.4.1406, 2000.

Engling, G., Zhang, Y.-N., Chan, C.-Y., Sang, X.-F., Lin, M., Ho, K.-F., Li, Y.-S., Lin, C.-Y., and Lee, J. J.: Characterization and sources of aerosol particles over the southeastern Tibetan Plateau during the Southeast Asia biomass-burning season, Tellus B, 63, 117–128, https://doi.org/10.1111/j.1600-0889.2010.00512.x, 2011.

Fast, J. D., de Foy, B., Acevedo Rosas, F., Caetano, E., Carmichael, G., Emmons, L., McKenna, D., Mena, M., Skamarock, W., Tie, X., Coulter, R. L., Barnard, J. C., Wiedinmyer, C., and Madronich, S.: A meteorological overview of the MILAGRO field campaigns, Atmos. Chem. Phys., 7, 2233–2257, https://doi.org/10.5194/acp-7-2233-2007, 2007.

Gysel, M., Laborde, M., Olfert, J. S., Subramanian, R., and Grohn, A. J.: Effective density of Aquadag and fullerene soot black carbon reference materials used for SP2 calibration, Atmos. Meas. Tech., 4, 2851–2858, https://doi.org/10.5194/amt-4-2851-2011, 2011.

He, C., Li, Q., Liou, K.-N., Takano, Y., Gu, Y., Qi, L., Mao, Y., and Leung, L. R.: Black carbon radiative forcing over the Tibetan Plateau, Geophys. Res. Lett., 41, 7806–7813, https://doi.org/10.1002/2014GL062191, 2014.

Hsu, Y.-K., Holsen, T. M., and Hopke, P. K.: Comparison of hybrid receptor models to locate PCB sources in Chicago, Atmos. Environ., 37, 545–562, https://doi.org/10.1016/S1352-2310(02)00886-5, 2003.

Huang, X. F., Sun, T. L., Zeng, L. W., Yu, G. H., and Luan, S. J.: Black carbon aerosol characterization in a coastal city in South China using a single particle soot photometer, Atmos. Environ., 51, 21–28, https://doi.org/10.1016/j.atmosenv.2012.01.056, 2012.

Huintjes, E., Loibl, D., Lehmkuhl, F., and Schneider, C.: A modelling approach to reconstruct Little Ice Age climate from remote-sensing glacier observations in southeastern Tibet, Ann. Glaciol., 57, 359–370, https://doi.org/10.3189/2016AoG71A025, 2016.

Immerzeel, W. W., van Beek, L. P. H., and Bierkens, M. F. P.: Climate change will affect the Asian water towers, Science, 328, 1382–1385, https://doi.org/10.1126/science.1183188, 2010.

Jacobson, M. Z.: Strong radiative heating due to the mixing state of black carbon in atmospheric aerosols, Nature, 409, 695–697, https://doi.org/10.1038/35055518, 2001.

Kang, S., Mayewski, P. A., Qin, D., Yan, Y., Zhang, D., Hou, S., and Ren, J.: Twentieth century increase of atmospheric ammonia recorded in Mount Everest ice core, J. Geophys. Res., 107, 4595, https://doi.org/10.1029/2001JD001413, 2002.

Kang, S., Wang, F., Morgenstern, U., Zhang, Y., Grigholm, B., Kaspari, S., Schwikowski, M., Ren, J., Yao, T., Qin, D., and Mayewski, P. A.: Dramatic loss of glacier accumulation area on the Tibetan Plateau revealed by ice core tritium and mercury records, The Cryosphere, 9, 1213–1222, https://doi.org/10.5194/tc-9-1213-2015, 2015.

Ke, L., Ding, X., Li, W., and Qiu, B.: Remote sensing of glacier change in the central Qinghai-Tibet Plateau and the relationship with changing climate, Remote Sens., 9, 114–133, https://doi.org/10.3390/rs9020114, 2017.

Laborde, M., Mertes, P., Zieger, P., Dommen, J., Baltensperger, U., and Gysel, M.: Sensitivity of the Single Particle Soot Photometer to different black carbon types, Atmos. Meas. Tech., 5, 1031–1043, https://doi.org/10.5194/amt-5-1031-2012, 2012.

Laskin, A., Laskin, J., and Nizkorodov, S. A.: Chemistry of atmospheric brown carbon, Chem. Rev., 115, 4335–4382, https://doi.org/10.1021/cr5006167, 2015.

Lau, K. M. and Kim, K. M.: Observational relationships between aerosol and Asian monsoon rainfall, and circulation, Geophys. Res. Lett., 33, L21810, https://doi.org/10.1029/2006GL027546, 2006.

Li, C., Bosch, C., Kang, S., Andersson, A., Chen, P., Zhang, Q., Cong, Z., Chen, B., Qin, D., and Gustafsson, Ö.: Sources of black carbon to the Himalayan–Tibetan Plateau glaciers, Nat. Commun., 7, 12574, https://doi.org/10.1038/ncomms12574, 2016a.

Li, C., Yan, F., Kang, S., Chen, P., Hu, Z., Gao, S., Qu, B., and Sillanpää, M.: Light absorption characteristics of carbonaceous aerosols in two remote stations of the southern fringe of the Tibetan Plateau, China, Atmos. Environ., 143, 79–85, 2016b.

Li, C., Chen, P., Kang, S., Yan, F., Hu, Z., Qu, B., and Sillanpää, M.: Concentrations and light absorption characteristics of carbonaceous aerosol in $PM_{2.5}$ and PM_{10} of Lhasa city, the Tibetan Plateau, Atmos. Environ., 127, 340–346, 2016c.

Li, C., Yan, F., Kang, S., Chen, P., Han, X., Hu, Z., Zhang, G., Hong, Y., Gao, S., Qu, B., Zhu, Z., Li, J., Chen, B., and Sillanpää, M.: Re-evaluating black carbon in the Himalayas and the Tibetan Plateau: concentrations and deposition, Atmos. Chem. Phys., 17, 11899–11912, https://doi.org/10.5194/acp-17-11899-2017, 2017.

Liu, D., Flynn, M., Gysel, M., Targino, A., Crawford, I., Bower, K., Choularton, T., Juranyi, Z., Steinbacher, M., Hueglin, C., Curtius, J., Kampus, M., Petzold, A., Weingartner, E., Baltensperger, U., and Coe, H.: Single particle characterization of black carbon aerosols at a tropospheric alpine site in Switzerland, Atmos. Chem. Phys., 10, 7389–7407, https://doi.org/10.5194/acp-10-7389-2010, 2010.

Liu, S., Aiken, A. C., Gorkowski, K., Dubey, M. K., Cappa, C. D., Williams, L. R., Herndon, S. C., Massoli, P., Fortner, E. C., Chhabra, P. S., Brooks, W. A., Onasch, T. B., Jayne, J. T., Worsnop, D. R., China, S., Sharma, N., Mazzoleni, C., Xu, L., Ng, N. L., Liu, D., Allan, J. D., Lee, J. D., Fleming, Z. L., Mohr, C., Zotter, P., Szidat, S., and Prevot, A. S. H.: Enhanced light absorption by mixed source black and brown carbon particles in UK winter, Nat. Commun., 6, 8435, https://doi.org/10.1038/ncomms9435, 2015.

Loibl, D., Lehmkuhl, F., and Grießinger, J.: Reconstructing glacier retreat since the Little Ice Age in SE Tibet by glacier mapping and equilibrium line altitude calculation, Geomorphology, 214, 22–39, https://doi.org/10.1016/j.geomorph.2014.03.018, 2014.

Lu, Z., Streets, D. G., Zhang, Q., and Wang, S.: A novel back-trajectory analysis of the origin of black carbon transported to the Himalayas and Tibetan Plateau during 1996–2010, Geophys. Res. Lett., 39, L01809, https://doi.org/10.1029/2011GL049903, 2012.

Ma, J. Z., Tang, J., Li, S. M., and Jacobson, M. Z.: Size distributions of ionic aerosols measured at Waliguan Observatory: Implication for nitrate gas-to-particle transfer processes in the free troposphere, J. Geophys. Res., 108, 4541, https://doi.org/10.1029/2002JD003356, 2003.

Marinoni, A., Cristofanelli, P., Laj, P., Duchi, R., Calzolari, F., Decesari, S., Sellegri, K., Vuillermoz, E., Verza, G. P., Villani, P., and Bonasoni, P.: Aerosol mass and black carbon concentrations, a two year record at NCO-P (5079 m, Southern Himalayas), Atmos. Chem. Phys., 10, 8551–8562, https://doi.org/10.5194/acp-10-8551-2010, 2010.

McMeeking, G. R., Morgan, W. T., Flynn, M., Highwood, E. J., Turnbull, K., Haywood, J., and Coe, H.: Black carbon aerosol mixing state, organic aerosols and aerosol optical properties over the United Kingdom, Atmos. Chem. Phys., 11, 9037–9052, https://doi.org/10.5194/acp-11-9037-2011, 2011.

Moosmüller, H., Chakrabarty, R. K., Ehlers, K. M., and Arnott, W. P.: Absorption Ångström coefficient, brown carbon, and aerosols: basic concepts, bulk matter, and spherical particles, Atmos. Chem. Phys., 11, 1217–1225, https://doi.org/10.5194/acp-11-1217-2011, 2011.

Pant, P., Hegde, P., Dumka, U. C., Sagar, R., Satheesh, S. K., Moorthy, K. K., Saha, A., and Srivastava, M. K.: Aerosol characteristics at a high-altitude location in central Himalayas: Optical properties and radiative forcing, J. Geophys. Res., 111, D17206, https://doi.org/10.1029/2005JD006768, 2006.

Peng, J. F., Hu, M., Guo, S., Du, Z. F., Zheng, J., Shang, D. J., Zamora, M. L., Zeng, L. M., Shao, M., Wu, Y. S., Zheng, J., Wang, Y., Glen, C. R., Collins, D. R., Molina, M. J., and Zhang, R. Y.: Markedly enhanced absorption and direct radiative forcing of black carbon under polluted urban environments, P. Natl. Acad. Sci. USA, 113, 4266–4271, https://doi.org/10.1073/pnas.1602310113, 2016.

Petzold, A., Ogren, J. A., Fiebig, M., Laj, P., Li, S.-M., Baltensperger, U., Holzer-Popp, T., Kinne, S., Pappalardo, G., Sugimoto, N., Wehrli, C., Wiedensohler, A., and Zhang, X.-Y.: Recommendations for reporting "black carbon" measurements, Atmos. Chem. Phys., 13, 8365–8379, https://doi.org/10.5194/acp-13-8365-2013, 2013.

Ping, X., Jiang, Z., and Li, C.: Status and future perspectives of energy consumption and its ecological impacts in the Qinghai–Tibet region, Renew. Sustain. Energ. Rev., 15, 514–523, https://doi.org/10.1016/j.rser.2010.07.037, 2011.

Raatikainen, T., Brus, D., Hyvärinen, A. P., Svensson, J., Asmi, E., and Lihavainen, H.: Black carbon concentrations and mixing state in the Finnish Arctic, Atmos. Chem. Phys., 15, 10057–10070, https://doi.org/10.5194/acp-15-10057-2015, 2015.

Raatikainen, T., Brus, D., Hooda, R. K., Hyvarinen, A.-P., Asmi, E., Sharma, V. P., Arola, A., and Lihavainen, H.: Size-selected black carbon mass distributions and mixing state in polluted and clean environments of northern India, Atmos. Chem. Phys., 17, 371–383, https://doi.org/10.5194/acp-17-371-2017, 2017.

Ramanathan, V. and Carmichael, G.: Global and regional climate changes due to black carbon, Nat. Geosci., 1, 221–227, https://doi.org/10.1038/ngeo156, 2008.

Sahu, L. K., Kondo, Y., Moteki, N., Takegawa, N., Zhao, Y., Cubison, M. J., Jimenez, J. L., Vay, S., Diskin, G. S., Wisthaler, A., Mikoviny, T., Huey, L. G., Weinheimer, A. J., and Knapp, D. J.: Emission characteristics of black carbon in anthropogenic and biomass burning plumes over California during ARCTAS-CARB 2008, J. Geophys. Res., 117, D16302, https://doi.org/10.1029/2011JD017401, 2012.

Schwarz, J. P., Gao, R. S., Fahey, D. W., Thomson, D. S., Watts, L. A., Wilson, J. C., Reeves, J. M., Darbeheshti, M., Baumgardner, D. G., Kok, G. L., Chung, S. H., Schulz, M., Hendricks, J., Lauer, A., Karcher, B., Slowik, J. G., Rosenlof, K. H., Thompson, T. L., Langford, A. O., Loewenstein, M., and Aikin, K. C.: Single-particle measurements of midlatitude black carbon and light-scattering aerosols from the boundary

layer to the lower stratosphere, J. Geophys. Res., 111, D16207, https://doi.org/10.1029/2006JD007076, 2006.

Schwarz, J. P., Gao, R. S., Spackman, J. R., Watts, L. A., Thomson, D. S., Fahey, D. W., Ryerson, T. B., Peischl, J., Holloway, J. S., Trainer, M., Frost, G. J., Baynard, T., Lack, D. A., de Gouw, J. A., Warneke, C., and Del Negro, L. A.: Measurement of the mixing state, mass, and optical size of individual black carbon particles in urban and biomass burning emissions, Geophys. Res. Lett., 35, L13810, https://doi.org/10.1029/2008GL033968, 2008.

Sirois, A. and Bottenheim, J. W.: Use of backward trajectories to interpret the 5-year record of PAN and O3 ambient air concentrations at Kejimkujik National Park, Nova Scotia, J. Geophys. Res., 100, 2867–2881, https://doi.org/10.1029/94JD02951, 1995.

Slowik, J. G., Cross, E. S., Han, J. H., Davidovits, P., Onasch, T. B., Jayne, J. T., Williams, L. R., Canagaratna, M. R., Worsnop, D. R., Chakrabarty, R. K., Moosmuller, H., Arnott, W. P., Schwarz, J. P., Gao, R. S., Fahey, D. W., Kok, G. L., and Petzold, A.: An inter-comparison of instruments measuring black carbon content of soot particles, Aerosol Sci. Tech., 41, 295–314, https://doi.org/10.1080/02786820701197078, 2007.

Stone, E. A., Schauer, J. J., Pradhan, B. B., Dangol, P. M., Habib, G., Venkataraman, C., and Ramanathan, V.: Characterization of emissions from South Asian biofuels and application to source apportionment of carbonaceous aerosol in the Himalayas, J. Geophys. Res., 115, D06301, https://doi.org/10.1029/2009JD011881, 2010.

Taylor, J. W., Allan, J. D., Allen, G., Coe, H., Williams, P. I., Flynn, M. J., Le Breton, M., Muller, J. B. A., Percival, C. J., Oram, D., Forster, G., Lee, J. D., Rickard, A. R., Parrington, M., and Palmer, P. I.: Size-dependent wet removal of black carbon in Canadian biomass burning plumes, Atmos. Chem. Phys., 14, 13755-13771, https://doi.org/10.5194/acp-14-13755-2014, 2014.

Vadrevu, K. P., Ohara, T., and Justice, C.: Air pollution in Asia, Environ. Pollut., 195, 233–235, https://doi.org/10.1016/j.envpol.2014.09.006, 2014.

Virkkula, A., Makela, T., Hillamo, R., Yli-Tuomi, T., Hirsikko, A., Hameri, K., and Koponen, I. K.: A simple procedure for correcting loading effects of aethalometer data, J. Air Waste Manage. Assoc., 57, 1214–1222, https://doi.org/10.3155/1047-3289.57.10.1214, 2007.

Wan, X., Kang, S., Wang, Y., Xin, J., Liu, B., Guo, Y., Wen, T., Zhang, G., and Cong, Z.: Size distribution of carbonaceous aerosols at a high-altitude site on the central Tibetan Plateau (Nam Co Station, 4730 m a.s.l.), Atmos. Res., 153, 155–164, https://doi.org/10.1016/j.atmosres.2014.08.008, 2015.

Wang, M., Xu, B., Wang, N., Cao, J., Tie, X., Wang, H., Zhu, C., and Yang, W.: Two distinct patterns of seasonal variation of airborne black carbon over Tibetan Plateau, Sci. Total Environ., 573, 1041–1052, https://doi.org/10.1016/j.scitotenv.2016.08.184, 2016.

Wang, Q., Schwarz, J. P., Cao, J., Gao, R., Fahey, D. W., Hu, T., Huang, R. J., Han, Y., and Shen, Z.: Black carbon aerosol characterization in a remote area of Qinghai–Tibetan Plateau, western China, Sci. Total Environ., 479–480, 151–158, https://doi.org/10.1016/j.scitotenv.2014.01.098, 2014.

Wang, Q., Huang, R.-J., Zhao, Z., Zhang, N., Wang, Y., Ni, H., Tie, X., Han, Y., Zhuang, M., Wang, M., Zhang, J., Zhang, X., Dusek, U., and Cao, J.: Size distribution and mixing state of refractory black carbon aerosol from a coastal city in South China, Atmos. Res., 181, 163–171, https://doi.org/10.1016/j.atmosres.2016.06.022, 2016a.

Wang, Q., Huang, R.-J., Zhao, Z., Cao, J., Ni, H., Tie, X., Zhao, S., Su, X., Han, Y., Shen, Z., Wang, Y., Zhang, N., Zhou, Y., and Corbin, J. C.: Physicochemical characteristics of black carbon aerosol and its radiative impact in a polluted urban area of China, J. Geophys. Res.-Atmos., 121, 12505–12519, https://doi.org/10.1002/2016JD024748, 2016b.

Wang, Q., Zhao, Z., Tian, J., Zhu, C., Ni, H., Zhang, Y., Zhang, N., Shen, Z., Han, Y., and Cao, J.: Seasonal transport and dry deposition of black carbon aerosol in the Southeastern Tibetan Plateau, Aerosol Sci. Eng., 1, 160–168, https://doi.org/10.1007/s41810-017-0016-y, 2017.

Wang, Q. Y., Huang, R. J., Cao, J. J., Tie, X. X., Ni, H. Y., Zhou, Y. Q., Han, Y. M., Hu, T. F., Zhu, C. S., Feng, T., Li, N., and Li, J. D.: Black carbon aerosol in winter northeastern Qinghai-Tibetan Plateau, China: the source, mixing state and optical property, Atmos. Chem. Phys., 15, 13059–13069, https://doi.org/10.5194/acp-15-13059-2015, 2015a.

Wang, Q. Y., Gao, R., Cao, J., Schwarz, J., Fahey, D., Shen, Z., Hu, T., Wang, P., Xu, X., and Huang, R.-J.: Observations of high level of ozone at Qinghai Lake basin in the northeastern Qinghai-Tibetan Plateau, western China, J. Atmos. Chem., 72, 19–26, https://doi.org/10.1007/s10874-015-9301-9, 2015b.

Wang, Y. Q., Zhang, X. Y., and Draxler, R. R.: TrajStat: GIS-based software that uses various trajectory statistical analysis methods to identify potential sources from long-term air pollution measurement data, Environ. Model. Softw., 24, 938–939, https://doi.org/10.1016/j.envsoft.2009.01.004, 2009.

White, W., Anderson, J., Blumenthal, D., Husar, R., Gillani, N., Husar, J., and Wilson, W.: Formation and transport of secondary air pollutants: ozone and aerosols in the St. Louis urban plume, Science, 194, 187–189, https://doi.org/10.1126/science.959846, 1976.

Wu, Y., Zhang, R., Tian, P., Tao, J., Hsu, S. C., Yan, P., Wang, Q., Cao, J., Zhang, X., and Xia, X.: Effect of ambient humidity on the light absorption amplification of black carbon in Beijing during January 2013, Atmos. Environ., 124, 217–223, https://doi.org/10.1016/j.atmosenv.2015.04.041, 2016.

Xu, B. Q., Cao, J. J., Hansen, J., Yao, T. D., Joswia, D. R., Wang, N. L., Wu, G. J., Wang, M., Zhao, H. B., Yang, W., Liu, X. Q., and He, J. Q.: Black soot and the survival of Tibetan glaciers, P. Natl. Acad. Sci. USA, 106, 22114–22118, https://doi.org/10.1073/pnas.0910444106, 2009.

Yao, T., Ren, J., and Xu, B.: Map of glaciers and lakes on the Tibetan Plateau and the surroundings, Xi'an Cartographic Publishing House, Xi'an, 2008.

Yao, T., Thompson, L., Yang, W., Yu, W., Gao, Y., Guo, X., Yang, X., Duan, K., Zhao, H., Xu, B., Pu, J., Lu, A., Xiang, Y., Kattel, D. B., and Joswiak, D.: Different glacier status with atmospheric circulations in Tibetan Plateau and surroundings, Nat. Clim. Change, 2, 663–667, https://doi.org/10.1038/nclimate1580, 2012.

Zhang, M., Wang, S., Li, Z., and Wang, F.: Glacier area shrinkage in China and its climatic background during the past half century, J. Geogr. Sci., 22, 15–28, https://doi.org/10.1007/s11442-012-0908-3, 2012.

Zhang, Q., Streets, D. G., Carmichael, G. R., He, K. B., Huo, H., Kannari, A., Klimont, Z., Park, I. S., Reddy, S., Fu, J. S., Chen, D., Duan, L., Lei, Y., Wang, L. T., and Yao, Z. L.: Asian emissions in 2006 for the NASA INTEX-B mission, Atmos. Chem. Phys., 9, 5131–5153, https://doi.org/10.5194/acp-9-5131-2009, 2009.

Zhang, R., Wang, H., Qian, Y., Rasch, P. J., Easter, R. C., Ma, P. L., Singh, B., Huang, J., and Fu, Q.: Quantifying sources, transport, deposition, and radiative forcing of black carbon over the Himalayas and Tibetan Plateau, Atmos. Chem. Phys., 15, 6205–6223, https://doi.org/10.5194/acp-15-6205-2015, 2015.

Zhang, X., Ming, J., Li, Z., Wang, F., and Zhang, G.: The online measured black carbon aerosol and source orientations in the Nam Co region, Tibet, Environ. Sci. Pollut. Res., 24, 25021–25033, 2017.

Zhang, Y., Zhang, Q., Cheng, Y., Su, H., Kecorius, S., Wang, Z., Wu, Z., Hu, M., Zhu, T., Wiedensohler, A., and He, K.: Measuring the morphology and density of internally mixed black carbon with SP2 and VTDMA: new insight into the absorption enhancement of black carbon in the atmosphere, Atmos. Meas. Tech., 9, 1833–1843, https://doi.org/10.5194/amt-9-1833-2016, 2016.

Zhang, Y., Kang, S., Li, C., Gao, T., Cong, Z., Sprenger, M., Liu, Y., Li, X., Guo, J., Sillanpää, M., Wang, K., Chen, J., Li, Y., and Sun, S.: Characteristics of black carbon in snow from Laohugou No. 12 glacier on the northern Tibetan Plateau, Sci. Total Environ., 607–608, 1237–1249, https://doi.org/10.1016/j.scitotenv.2017.07.100, 2017.

Zhao, S., Ming, J., Xiao, C., Sun, W., and Qin, X.: A preliminary study on measurements of black carbon in the atmosphere of northwest Qilian Shan, J. Environ. Sci., 24, 152–159, https://doi.org/10.1016/S1001-0742(11)60739-0, 2012.

Zhao, S., Tie, X., Long, X., and Cao, J.: Impacts of Himalayas on black carbon over the Tibetan Plateau during summer monsoon, Sci. Total Environ., 598, 307–318, https://doi.org/10.1016/j.scitotenv.2017.04.101, 2017.

Zhao, Z., Wang, Q., Xu, B., Shen, Z., Huang, R., Zhu, C., Su, X., Zhao, S., Long, X., Liu, S., and Cao, J.: Black carbon aerosol and its radiative impact at a high-altitude remote site on the southeastern Tibet Plateau, J. Geophys. Res.-Atmos., 122, 1–16, https://doi.org/10.1002/2016JD026032, 2017.

Zhu, C.-S., Cao, J.-J., Xu, B.-Q., Huang, R.-J., Wang, P., Ho, K.-F., Shen, Z.-X., Liu, S.-X., Han, Y.-M., Tie, X.-X., Zhao, Z.-Z., and Chen, L. W. A.: Black carbon aerosols at Mt. Muztagh Ata, a high-altitude location in the Western Tibetan Plateau, Aerosol Air Qual. Res., 16, 752–763, https://doi.org/10.4209/aaqr.2015.04.0255, 2016.